Journal of Polymers and the Environment (2024) 32:4440–4455
https://doi.org/10.1007/s10924-024-03219-3

ORIGINAL PAPER

Synthesis of Reusable CNF/Ag_2Se Films as Visible-Light-Driven Photocatalysts for Photocatalytic Degradation of MB

Talaat A. Hameed[1] · Ahmed Salama[2] · Rabab A. Nasr[3]

Accepted: 17 February 2024 / Published online: 4 April 2024

Abstract

In our study's scenario, flexible films were fabricated from TEMPO-oxidized cellulose nanofibers and silver selenide (CNF/Ag_2Se) as efficient membranes for the degradation of methylene blue (MB). Different concentrations of Ag_2Se particles were in situ prepared in the presence of CNF. The in-situ synthesis of Ag_2Se nanoparticles in the presence of CNF was reported as efficient technique for the formation of submicrosize Ag_2Se particles with a narrow size distribution and homogeneous dispersion onto CNF. TEM analysis revealed that the nanofibers had uniform width and diameter, while XRD demonstrated single-phase orthorhombic β-Ag_2Se formation. 3D-FESEM showed tiny root measurer values of 28, 30, and 32.56 nm in polymeric films with 2.5, 5, and 10% Ag_2Se-filled CNF. Polymeric films had visible-driven-light photocatalytic activity because the band gap fell from 4.61 eV (UV area) to 2.71 eV (visible region). The composite's photocatalytic performance was assessed by MB degradation. 10% of CNF/Ag_2Se demonstrated maximal photocatalytic activity under simulated sunlight for 60 min, pH 9, and 3 g/L composite weight. The factorial design statistical analysis showed that MB dye photodegradation is mostly affected by irradiation time and dye concentration. Environmental, social, and economic factors are all considered, making this study suitable for implementing photocatalysis to large-scale water treatment systems, which is a key component of sustainability.

Keywords Cellulose nanofibers · Silver selenide · Optical properties · Visible light photocatalytic degradation

Introduction

One of the potential strategies for treating wastewater including organic pollutants is photocatalytic degradation. The substantial photo-redox potential and high photo-excitation probability of several semiconductors makes them excellent candidates for photocatalytic processes with environmental applications. In particular, they have been implemented in the removal of organic pollutants from wastewater because it yields the highest efficiency and reusability [1–4].

In the ongoing state of research, semiconductors are materials that have intermediate conductivity compared to metals and insulators [5–9]. Metal oxides and chalcogenides are two of the extensively researched semiconductor materials in many aspects [10]. Metal oxide including TiO_2 and ZnO is the most successful material employed in photocatalysis owing to it is high stability and resistance to photocorrosion [11]. Nevertheless, their wide band gap considers a big hurdle towards their commercialization because these classes of material absorb only in the UV region which only represented about 4% of the solar spectrum and thereupon many researchers have been devoted to developing materials with a narrow band gap energy that can absorb the visible region which meets the solar apex [12, 13].

Chalcogenides have exhibited many attributes over famous metal oxides, for example, it possesses very narrow band gap meeting visible light absorption, they are inexpensive, and have a high density of states which increase the probability of being excited, have a great intention for doping and modifications [14]. Contrary to metal oxide, metal chalcogenides possess a multifarious architecture that can be

✉ Ahmed Salama
ahmed_nigm78@yahoo.com

[1] Solid-State Physics Department, Physics Research Institute, National Research Centre, 33 El Bohouth St., Dokki, Giza 12622, Egypt

[2] Cellulose and Paper Department, National Research Centre, 33 El-Bohouth St., Dokki, P.O. 12622, Giza, Egypt

[3] Department of Water Pollution Research, National Research Centre, 33 El Bohouth St., Dokki, Giza 12622, Egypt

enriched by the inclusion of different metal ions and templates thereby controlling all the physical and chemical properties including the optical and electrical properties [6]. All These merits nominate the chalcogenides as an ideal alternative to metal oxide in photocatalysis [15]. Chalcogenides are a class of compounds that are formed from chalcogen (S, Se, and Te) and at least one electropositive element (Ag, Cu, etc.) [16]. Owing to these significant and unique properties, chalcogenides have been employed in tremendous application, including but not limited to solar cells optoelectronics [17, 18], piezoelectric, thermoelectric [19], transducers [20], supercapacitor [21], sensors [22], photocatalysis [23], and hydrogen generation [24].

As a rule, plenty of chalcogenides have been explored as photocatalysts, to name a few, simple sulfides (e.g., Sb_2S_3 [25], In_2S_3 [26] and ZnS_5 [27]), complex sulfides ($ZnIn_2S_4$ [28], ZnCdS [29] and $AgIn_5S_8$ [30]). Thanks to their unique electronic structure, two-dimensional transition-metal dichalcogenides; for example, W_2S [31], MoSe [32], and $TiSe_2$ [3] have been extensively investigated in photocatalysis applications.

Out of all reported metal chalcogenides, Ag_2Se stands quite different because of featured physical and chemical properties like stable phase structures, narrow band gap, high absorption coefficient, and facile preparation [3, 33]. Ag_2Se formed in two stable phase structures. The high-temperature cubic phase (β-Ag_2Se) shows great success in photoelectric secondary batteries' multifunctional ion-selective electrodes. The low-temperature orthorhombic phase can be worked in photosensitizer in optical material and photocatalysis. Yang et al. reported the high photocatalytic performance of AgCl/Ag_2Se in the degradation of malachite green (MG) dyes [34]. Zhong et al. demonstrated the core–shell Ag@AgSex nanoparticles an excellent H_2-generation rate of Ag nanoparticles in a TiO_2/Ag system [3]. Nevertheless, its narrow band gap increases the recombination at the surface which underrated their photocatalytic performance. The high price of Ag_2Se that required high amounts of Ag_2Se, which render the commercialization is very difficult. Besides, these classes of material are easily oxidized which results in impeding the photocatalysis process.

Photocatalytic nanoparticles have been utilized extensively for wastewater treatment in a slurry reactor [35]. However, reusing nanoparticles from wastewater processed should increase expenditures on operations and reduce reaction performance. Additionally, nanoparticle release into the environment may create secondary contaminants. To optimize their reactivity and reuse rate, catalytic nanoparticles should be immobilized without aggregation and released from the reactor. Glass activated carbon particles and silica gel have been used to immobilize metals and metal oxide nanoparticles as catalyst [36]. Recently, extensive trials have been carried out for immobilization of metals nanoparticles onto polymers for various applications [37, 38].

The effective scenario to fill the above-mentioned gaps is the incorporation of Ag_2Se inside host polymeric materials and employing it as an immobilized photocatalyst for pollutants degradation under simulated sun light, using methylene blue dye as an example for organic contaminant in wastewater. In a broader sense, Nanoparticle-polymer composites are highly seen as the charming solution for renovated material holding unexpected features compared to their hosts [39]. Nanocellulose materials, such as cellulose nanofibers, and their derivatives have been prepared from the most abundant, and renewable biopolymer, i.e., cellulose, on the earth [40]. These biomaterials have distinctive physicochemical properties such as high tensile strength, large elastic modulus, and low density [41]. Cellulose nanofibers (CNF) with a high surface-to-volume ratio have been prepared from the (2,2,6,6-tetramethylpiperidiniyl-1-oxyl)-oxidation (TEMPO) method, which causes a lesser extent of degradation of the amorphous structure than the acidic hydrolysis process of cellulose nanocrystals. They are accordingly applied in various applications such as reinforcing fillers optical materials, electroconductive materials, and biomedical applications. For example, a flexible thermoelectric paper was prepared from bacterial cellulose/silver selenide nanocomposites. Ag_2Se nanoparticles were in situ synthesized in the network of bacterial cellulose. The results showed that the in-situ synthesis produces nanosized Ag_2Se particles with a narrow size distribution and homogeneous dispersion in the nanofiber network [42].

In this contribution, for the first time, we reported on the development of CNF/Ag_2Se films. First, the inclusion of silver selenide into the CNF matrix will result in the formation of a flexible film polymer that can find wider applications than Ag_2Se alone, for example as a passivating layer in supercapacitor. Second, the resultant CNF/Ag_2Se films will decrease the recombination of the Ag_2Se which works as a barrier to prevent the return of the electron. Finally, we found that a small amount of Ag_2Se is enough to reach the band gap in the visible region and the enhancement of photocatalytic performance, accordingly. For the first time, this work unravels the structural, composition, optical properties and photocatalytic performance of this CNF/xAg_2Se film.

2- Experimental

Materials

Ascorbic acid (99.0%), silver nitrate (99.8%) and sodium selenite (Na_2SeO_3) were purchased from Sigma. All the chemicals were used as received without further purification.

CNF Preparation

As previously described [40], cellulose nanofibers were produced from bleached bagasse pulp by TEMPO-oxidation and mechanical defibrillation with a grinder (Masuko Sangyo Co. Ltd., Japan). 4 g of bleached bagasse pulp were treated with a solution containing 0.16 g of TEMPO and 1.6 g of sodium bromide in 600 mL of distilled water followed by adding 60 mL of sodium hypochlorite. At the end of the reaction the pH was adjusted to 7 and the prepared CNF was separated by centrifuging followed by washing with water and dialysis for 7 days against deionized water. Mechanical defibrillation was used to obtain CNF. The results displayed that CNF has a carboxylate content of 1.3 ± 0.3 mmol/g as determined by electric conductivity titration.

Preparation of CNF/Ag_2Se

CNF/Ag_2Se was fabricated by in situ synthesis of Ag_2Se nanoparticles in the structure of CNF. To prepare CNF/Ag_2Se nanocomposites, ascorbic acid was used as reducing agent and CNF was used as supporting biopolymer. For this purpose, 10 mL of CNF was poured into 100-mL flasks containing 40 mL of distilled water. Then appropriate amounts of silver nitrate ($AgNO_3$) and sodium selenite (Na_2SeO_3) were added to prepare CNF films containing 2.5, 5 and 10% of Ag_2Se which labeled as CNF/Ag_2Se I, CNF/Ag_2Se II and CNF/Ag_2Se III, respectively. The ascorbic acid solution was added under continuous stirring at 40 °C for 3 h. CNF/Ag_2Se nanocomposites were centrifuged at 13,000 rpm and washed by distilled water. Finally, the precipitate was dried at 40 °C in an oven for 24 h.

Experimental Setup of Photocatalytic Activity Performance

The photocatalytic efficiency of CNF/Ag_2Se composite films was evaluated using photodegradation of the model organic pollutant MB dye as a function of Ag_2Se loading for 2.5 to 10% Ag_2Se. A 20 mg/L solution of MB dye was swirled with a magnetic stirrer in a dark 200 mL beaker for 60 min to achieve adsorption–desorption equilibrium. The beaker was illuminated by simulated sunlight straight down. To test the decolorization's success, a 5-mL aliquot of the reaction solution was taken. Dye concentration was measured using a Cary-100 double-beam UV–Vis spectrophotometer, with a calibration curve established at a maximum wavelength of 663 nm; efficiency was calculated using the formula %removal = (C/Co)*100, where Co and C are the initial and final dye concentrations, respectively. The role of the HO· radical, photogenerated holes (h^+), and the $O_2^{-\cdot}$ radical in the photodegradation of MB dye was investigated by running experiments with 50 mmol of ethanol and adding EDTA scavenger to the reaction mixture individually. At the completion of the 10% CNF/Ag_2Se-based MB degrading experiment, a GC/MS analysis was carried out utilizing a Varian 4500, fused silica capillary column (30 m 0.25 mm, 0.25 m film thickness), electron ionization system, and ionization energy of 70 eV in full scan mode. Acute toxicity data were reported as Effective concentrations EC50 (mg/L) for the treated water, as required by ISO 11348-3, 2007. The luminescence suppressed by marine gram-negative bacteria is a foundation for the Microtox acute toxicity test. The strain of Lyophilized Vibrio fischeri (NRRLB-11177) was utilized in the experiment. Cosmically prepared with 2% NaCl, the bacterial suspension was incorporated to the sample and its dilutions. Periodic photometry measurement was performed after the bacteria were exposed to the sample. The low and high levels of each factor, as well as the matrix of the whole factorial design with removal efficiency values and fits, were depicted during the experimental design using Minitab 18 software. ANOVA software was used to analyze all of the factorial design statistical data.

Characterization

The crystallographic measurement and phase examination of the polymer and Ag_2Se nanofiller were recognized by X-ray diffraction (XRD) with a scan rate of 0.05 s^{-1} in the 2θ range from 20 to 80 by Bruker, D8 advance (Germany) X-ray diffractometer using CuK_α X-ray radiation ($\lambda = 0.15406$ nm). The UV–Vis-NIR absorption of the investigated films was recognized by a double beam spectrophotometer (SP, JASCO, V-570, Japan), which operates over the wavelength range of 190 to 2500 nm. Films were examined by field-emission scanning electron microscope (FESEM) equipped with an EDX detector (Quanta 250 FEG), which allowed for analysis of their surface morphology. Extracting the roughness features from FESEM images was done with the aid of Gwyddion software (3D micrographs). The photocatalysis (UVA CUBE 400, Dr Honle AG UV Technology, Germany) with a halogen lamp installed (model: SOL 500), simulates natural sunlight (1000 W m^{-2}).

Results and Discussion

Structure Analysis

Phase Identification

The phase structures of pristine CNF and CNF/xAg_2Se nanocomposites at different concentrations ($x = 2.5$, 5, and 10 wt% of Ag_2Se) were detected by X-ray diffractometer, as illustrated in Fig. 1a. The diffraction spectra of pure CNF displayed the typical cellulose crystalline structure of reflections at 16.4° and

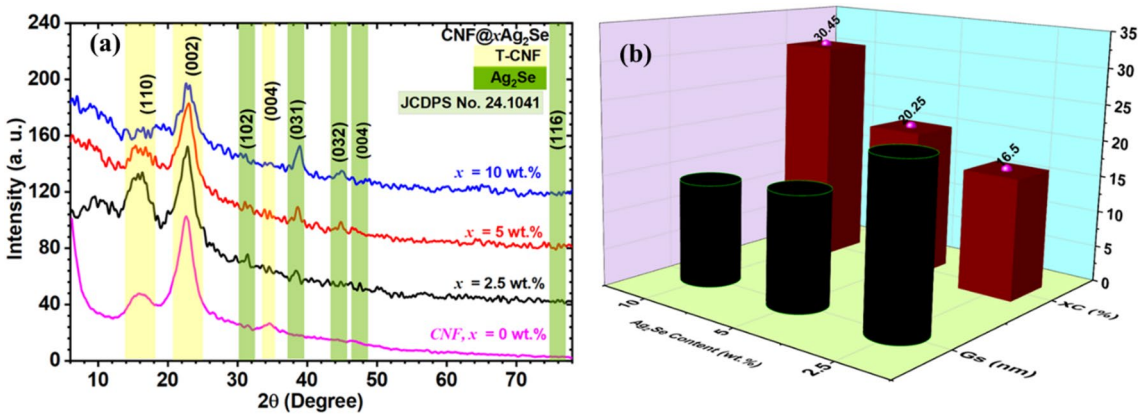

Fig.1 **a** XRD patterns of CNF and CNF/xAg_2Se and **b** the relation between Ag_2Se concentration and grain size and degree of crystallinity

22.5° that can be assigned to (101) and (002), respectively. The filled films with various wt% of Ag_2Se exhibited an intense diffraction line at 30.9, 39.9, 43.72, 48.05, and 78.08° which index to (102), (031), (032), (004), and (116), respectively according to the JCDPS No. 24.1041. Noticeably, it has been revealed the absence of any crystalline peaks for and secondary phase points out the high purity of Ag_2Se nanoparticles inside CNF. Therefore, Ag_2Se has been formed in single-phase orthorhombic β-Ag_2Se. Consequently, the lattice parameters (a, b, and c) of the orthorhombic β-Ag_2Se have been calculated according to Eq. (1) [43]:

$$\frac{1}{d^2} = \frac{h^2}{a^2} + \frac{k^2}{b^2} + \frac{l^2}{c^2} \tag{1}$$

The obtained values of lattice parameters are a = 4.313 Å, b = 7.042 Å, and c = 7.754 Å which are very consistent with the reported JCPDS No. 24.1041 (a = 4.33, b = 7.06, and c = 7.76) and some previously works [44].

The variation peak broadening and of the reflection intensity are a pewful sign of a change in grain size and degree of crystallinity (Xc); therefore, the crystallite size (DD-S) microstrain (ε), dislocation (ζ), number of crystallites (N), and degree of crystallinity (Xc) here has been evaluated according to the below equations [45–48]:

$$D_{D-S} = \frac{k\lambda}{\beta_{D-S}} \frac{1}{\cos(\theta)} \tag{2}$$

$$X_c = S/S_o \times 100 \tag{3}$$

$$\varepsilon = \frac{\beta}{4\tan(\theta)} \tag{4}$$

$$\delta = \frac{1}{D^2} \tag{5}$$

$$N = \frac{t}{D^3} \tag{6}$$

where t expresses the thickness of the films (1 mm), S refers to the area under the crystalline lines and S_o refers to the total area under the whole pattern. A representative relation between Ag_2Se concentration and grain size and degree of crystallinity is illustrated in Fig. 1b. The grain size decreased with the increase of silver selenide where the degree of crystallinity is boosted. First, the decrement in grain size is in favor of the photocatalytic application, which is the aim of this work, where it leads to an increase in the surface-to-volume ratio. The increase in the degree of crystallinity also will help the improvement of photocatalyst performance, because it enhances carrier transport. The values of microstrain (ε), dislocation (ζ), and number of crystallites (N) are recorded in Table 1.

Morphology and Composition

Figure 2a–c represents the morphologies of CNF/Ag_2Se nanocomposite with 2.5, 5, and 10 wt% of Ag_2Se and their corresponding 3D-view are represented in Fig. 2d–f. For all SEM images, it clears the presence of the CNF in the background that behaves like a long-connected filament which is rather different than pure CNF, which behaves like separate

Table 1 The values of grain size (G_s) in bold, microstrain (ε), dislocation (ζ), and number of crystallites (N) of CNF and the prepared films

CNF/xAgSe	Gs (nm)	X_c (nm)	$\varepsilon \times 10^{-3}$	$\delta \times 10^{11}$ (line/cm^3)	$N \times 10^{12}$
0	–	–	–	–	–
2.5	**22.52**	16.50	5.11	1.97	4.37
5	**15.41**	20.25	7.47	4.20	13.65
10	**13.94**	30.45	8.25	5.14	18.43

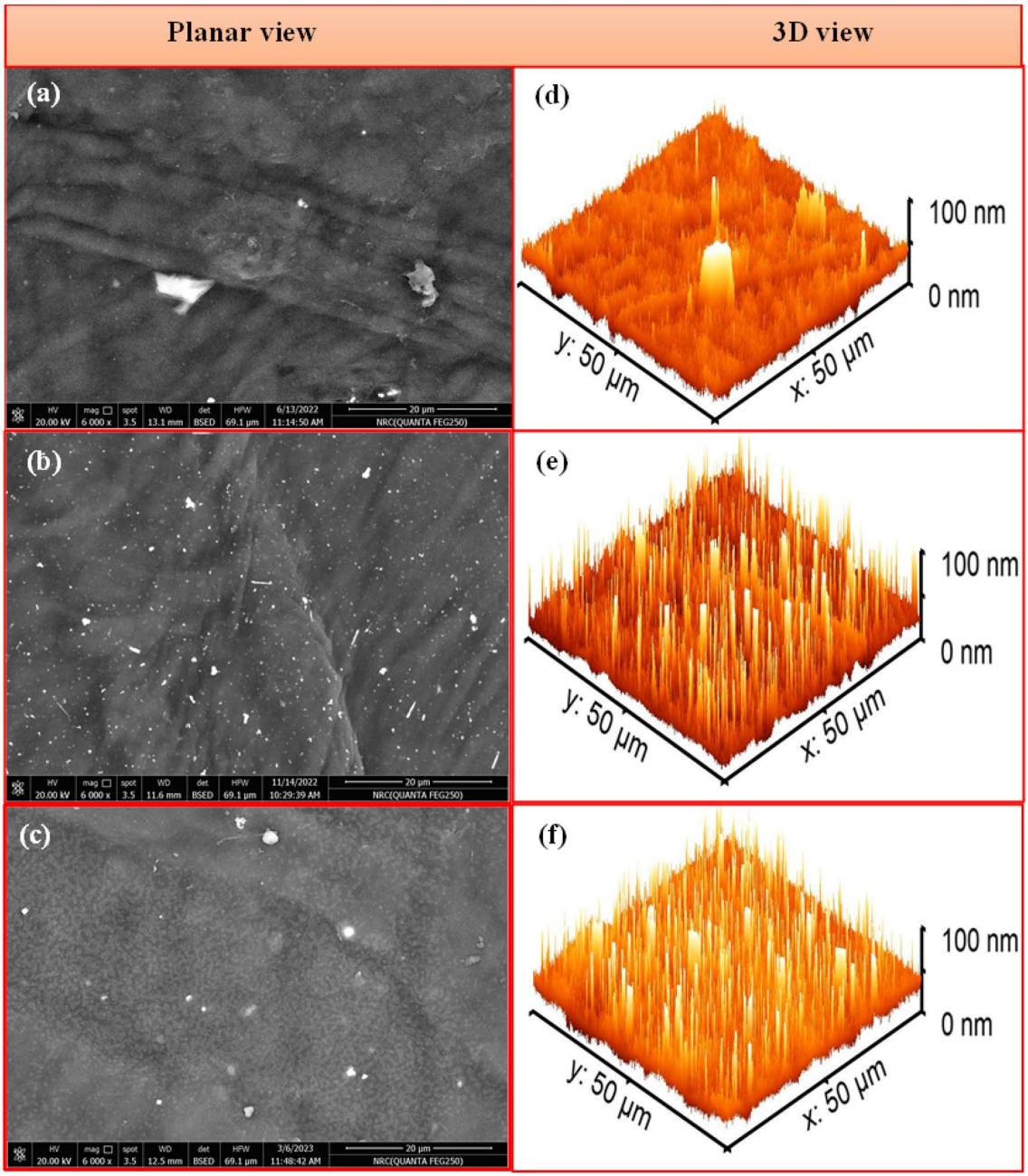

Fig. 2 SEM of CNF/Ag_2Se I (**A**), CNF/Ag_2Se II (**B**) and CNF/Ag_2Se III (**C**)

filaments and rods (Fig. 2c). This demonstrates the impact of Ag_2Se nanoparticle on the morphological feature of CNF. In addition, for the highest concentration of Ag_2Se, the filament completely disappeared, and morphology adopts semi-spherical shapes. The nanoparticles of Ag_2Se can be clearly seen at the surface of CNF which adopts aspherical and fine rod shapes. Moreover, the Ag_2Se particles are homogeneously dispersed within the CNF films. The SEM images confirm that using CNF, monodispersed Ag_2Se nanoparticles can be created with an average size of 45 nm with few agglomerated nanoparticles. This unique uniform size and distribution of the CNF/Ag_2Se nanocomposite benefits from the in-situ synthesis of Ag_2Se in the presence of CNF which limits the growth or the clustering of Ag_2Se nanoparticles. Such surface of the synthesized nanocomposite may be suitable if it is used as a photocatalyst for the degradation of dyes [49]. For further verification of this point, the 3D-FESEM view is represented in Fig. 2d–f, which confirmed that the polymeric films have a small root measurer value of about 28, 30, and 32.56 nm for 2.5, 5, and 10 wt% Ag_2Se-filled CNF.

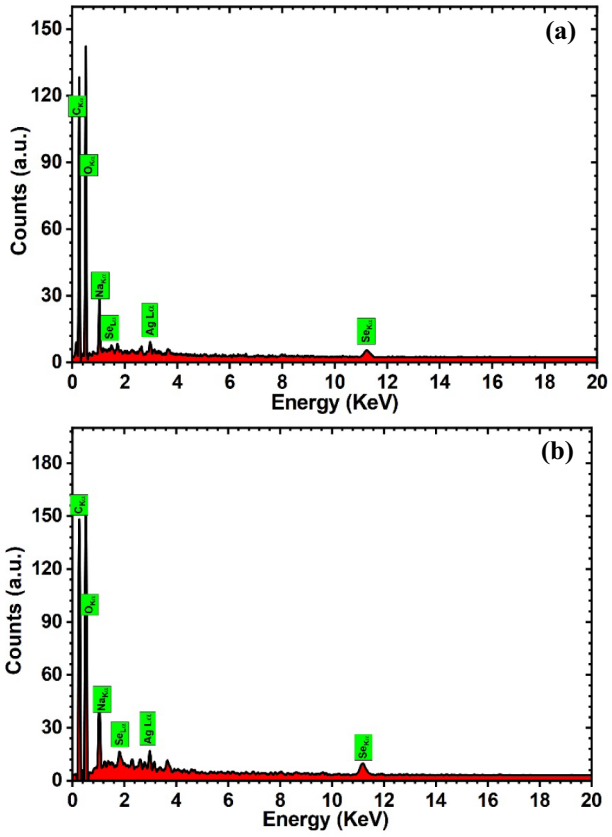

CNF/*x*AgSe	Elements	C	O	Na	Ag	Se
***x* = 2.5**	wt. %	44.58	45.47	5.70	1.30	2.95
	At. %	54.17	41.49	3.62	0.18	0.55
***x* = 10**	wt. %	43.19	45.24	4.78	3.78	3.01
	At. %	52.39	43.93	3.03	0.11	0.55

Fig. 3 EDX of CNF/Ag_2Se I (**a**), CNF/Ag_2Se III (**b**) and table displays the Wt and Atomic percentage of the elements

The energy-dispersive X-ray analysis was utilized for the qualitative and quantitative evaluation of nanocomposite polymeric films. Figure 3a–c depicted the EDAX spectra of CNF and Ag_2Se/xCNF nanocomposites (where x = 2.5, 5, and 10 wt%). The spectra show the presence of Ag, Se which collaborated with the successful inclusion of Ag_2Se into polymeric films. Also, the wt% obtained from EDX confirmed the right stoichiometry for these Ag_2Se nanoparticles.

The HRTEM microscopy was performed on the pure CNF and CNF/Ag_2Se nanocomposites synthesized by TEMPO-oxidation methods, as shown in Fig. 4a–c. The synthesis and microstructure of pure CNF was confirmed via the formation of very long nanofiber with different degree of entanglement and almost 45 nm in width (Fig. 4a). The in-situ synthesis of CNF/Ag_2Se shows a very different structure, where it sems like fluffy structure and the Ag_2Se nanoparticles are anchored on the surface of CNF which confirms that Ag_2Se may chemically contact with CNF (Fig. 4b, c). It is evident that Ag_2Se has a spherical and rectangular shape of particle size about 33.29 nm, which is very close to XRD measurement (Fig. 4c). The Selected area electron diffraction pattern (SAED) of the HRTEM shows a concentric diffraction ring with bright spots that established the crystalline nature of Ag_2Se which is consistent with XRD d observations.

Optical Study

The optical properties of the papered films, in particular, the band gap, plays a very essential key in evaluating the ability of the films in the photocatalytic application. Figure 5a represents the wavelength dependence of absorbance (A) for pristine CNF and CNF/xAg_2Se nanocomposites (where x = 2.5, 5, and 10 wt%). As illustrated, the CNF film has excellent transmittance within the UV–Vis-NIR visible wavelength range of 400–2500 nm, and all the transmittance remained above 80%. On the hand, it exhibits a sharp peak suited at 310 nm which is very close to the reported value at 340 nm. The slight difference originated from the variation of the nature of prepared cellulose, where Pervaiz et.al synthesized bulk cellulose and in this work, we prepared cellulose nanofiber which surely has a different band gap that causes the edge of absorbance peak to be shifted to a higher wavenumber [49]. It is worth mentioning that upon the addition of Ag_2Se fillers, the absorbance curves were enhanced, particularly in the region 490 to 550 nm which means that the absorbance of more electron UV–Vis region. On the other hand, an obvious red shift could be observed on the cut-off wavelength from 385 to 411 nm owing to the inclusion of Ag_2Se, which reflected the decrease in band gap which is the significant matter here to boost the photocatalytic performance.

The determination of band gap values provides the decision of functionalizing the film in photocatalysis and the region that it can work in it, where the visible light range is favorable owing to the high intensity of solar irradiance. The most reliable way for calculating the band gap is by taking into account the effect of transmittance and reflection together. The band gap of the prepared films can be calculated by using the famous Tauc's equations [12]:

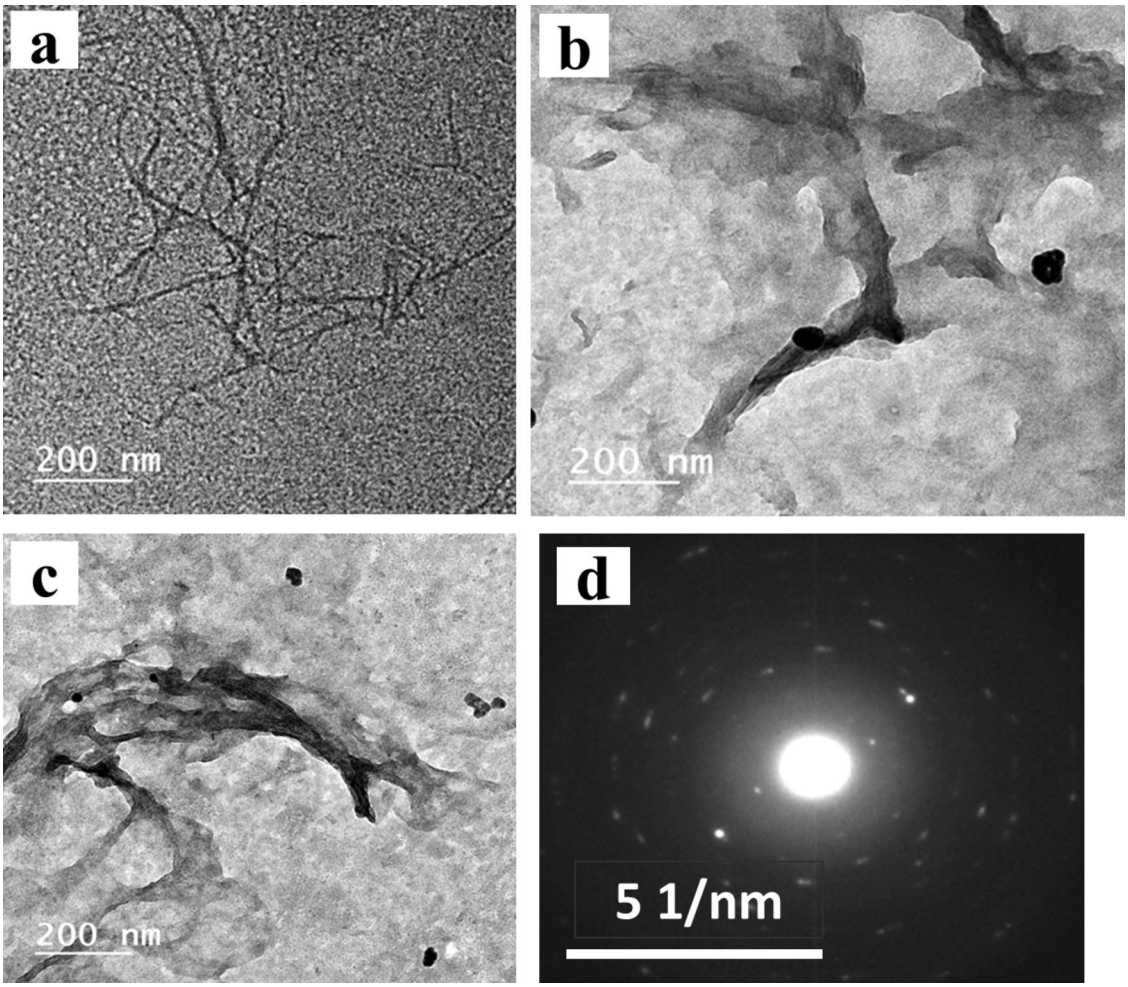

Fig. 4 TEM image of CNF (**a**) CNF/Ag_2Se I (**b**), CNF/Ag_2Se III (**c**) and SAED for CNF/Ag_2Se I (**d**)

$$\alpha h\nu = A\left(h\nu - E_g\right)^p \tag{7}$$

where υ expresses the frequency of, h refers to plank constant, E_g denotes the optical band gap, A implies constant relaying on effective masses associated with the band, and p is the parameter that defines the kind of transition which is direct transition and equal to 2. A is the bastion coefficient and can be determined from the below relation [50]:

$$\alpha = \frac{1}{d} log\left(\frac{1}{T}\right) \tag{8}$$

where t is the transmittance and d is the thickness of films. Values of the band gap energy (E_g) for the polymeric films can be determined from the extrapolation of the linear portion of the relation between $(\alpha h\nu)^2$ versus hν to the abscissa, as can be depicted in Fig. 5b–e. Moreover, Fig. 5f is a representation of the band gap against filler content, that demonstrated that the band gap is decreased upon the increase in Ag_2Se. It is worth noting that the band gap decreased from 4.61 eV (UV region) to 2.71 eV (visible region) which asserts the effectiveness of polymeric films in visible-driven-light photocatalytic activity.

Photocatalytic Activity

Dye Photocatalytic Degradation

The prepared films are used to degrade MB, and their effectiveness are determined by comparing the concentration drop to the concentration level at the start. Figure 6a shows the degradation% of MB as a function of contact time with the prepared nanocomposite films. It demonstrated that the

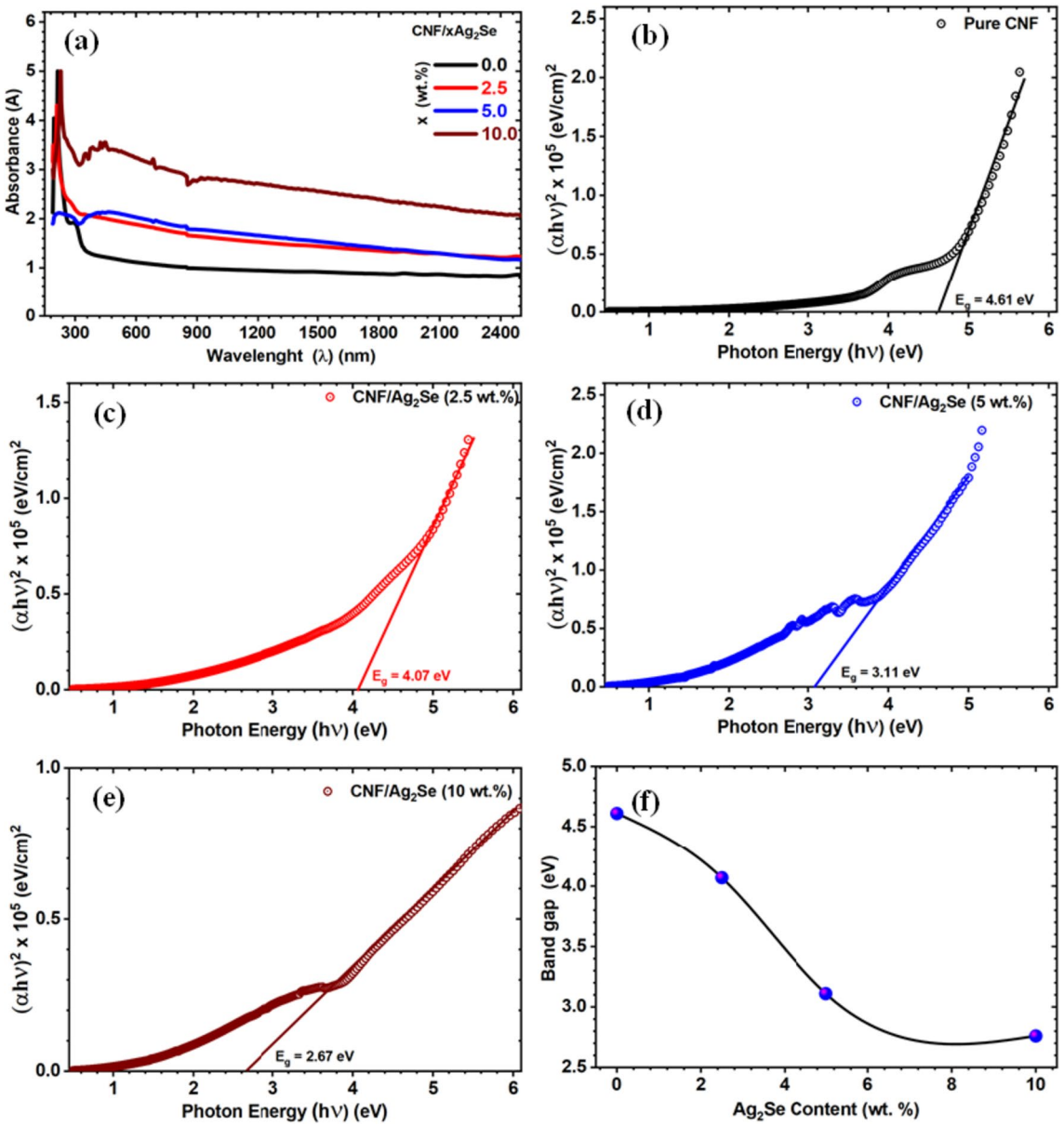

Fig. 5 **a** The spectral variation of the absorbance (A) as a function of wavelength; **b**–**e** the variation of, $(\alpha h\nu)^2$ photon energy hν for pure CNF, CNF/Ag_2Se I, CNF/Ag_2Se II and CNF/Ag_2Se III, respectively; and **f** The variation of optical direct band gap with Ag_2Se content

degradation of MB upon contact with Ag_2Se nanoparticles began immediately and increased over time till nearly steady condition. The degradation of the dye may be attributable to the breakdown of the chromophores responsible for its original color. Methylene blue dye photodegradation is proceeded by photogenerated holes (h^+) and the $O_2^{-\cdot}$ radical under visible light illumination [51]. At pH 7 and film weight 1 g/L, the effect of contact time (up to 60 min) was more obvious, 26.5%, 45%, 48.5% utilizing 2.5%, 5%, and 10% Ag_2Se composite films, respectively followed by slight enhanced in the degradation percent. Consequently, the 60 min was elected as the optimal illumination time. Keep in mind that no significant dye loss (< 2%) is seen in illuminated blank solution (without films). As well as, CNF can remove around 5% of a sample with no illumination at all (control degradation experiment). Here, the main hypothesis was that increasing Ag_2Se% (photocatalyst) could give higher active sites available for photodegradation. So, 10% Ag_2Se was elected as the composite with the highest photodegradation performance among the synthesized composite. In the other hand, the structure of cellulose also aids in the uniform distribution of Ag_2Se NPs across polymeric matrix, which improves the adsorption of the dye molecules and, potentially, the efficiency of the photodegradation process

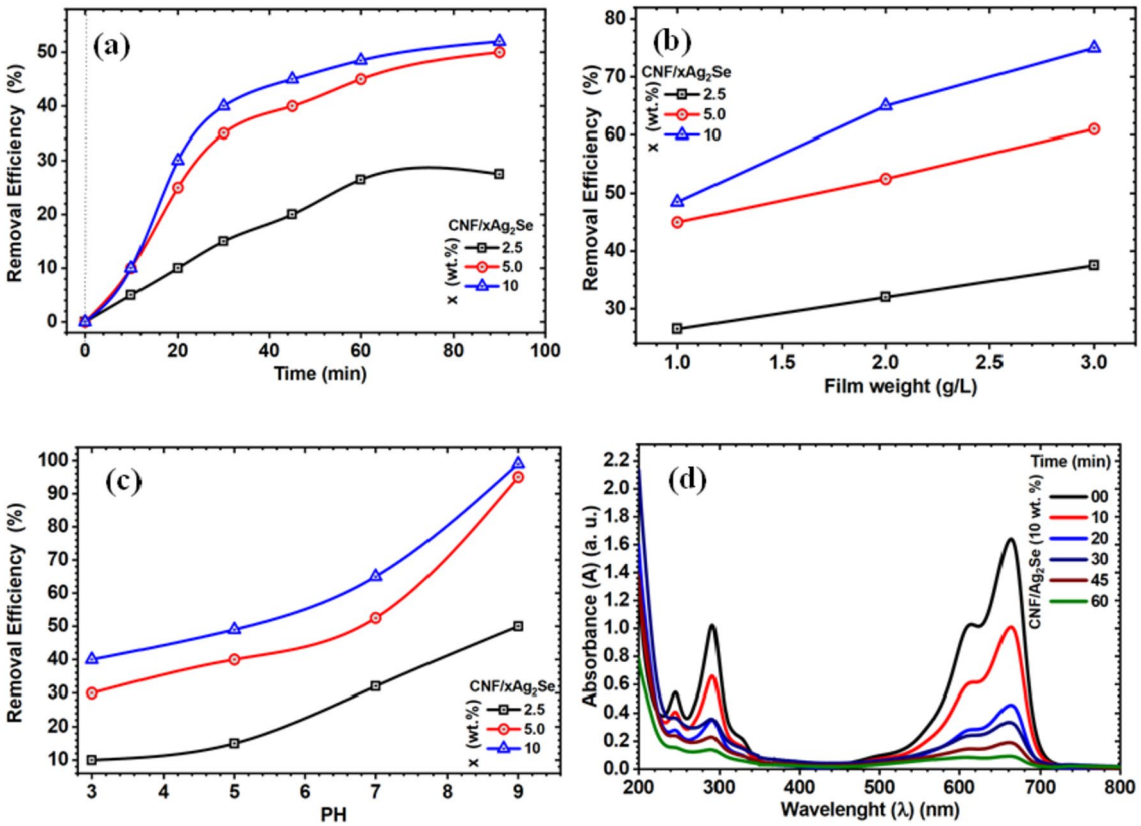

Fig. 6 **a** MB degradation at pH 7, 20 mg/L, and 1 g/L film weight as a function of irradiation duration, **b** MB degradation at pH 7, 20 mg/L and 60 min irradiation time as a function of film weight, **c** MB degradation at 20 mg/L, 3 g/L film weight and 60 min irradiation time as a function of pH and **d** UV–Vis studies of MB degradation using 10% Ag_2S film under optimum operating conditions

[52]. MB photocatalytic deterioration reflects the composites' decreasing band gap. Photocatalytic activity may be increased by better electron–hole pair separation. Photogenerated electrons and holes transfer to the composite surface to react with the dye molecule, limiting electron–hole recombination [53, 54].

The percentage of degradation after 60 min of simulated sunlight was compared with different amounts of composite material (Fig. 6b). All prepared composites show an increase in photodegradation as their composite weight is increased from 1 to 3 gm at pH 7. Moreover, 3 g/L of 10% CNF/Ag_2Se were able to degrade 75% of the MB which is the composite with higher photodegradation rate among all prepared composites. The basic assumption here was that adding more Ag_2Se% (photocatalyst) to the composite as its weight increased would result in more active sites available for photodegradation.

Figure 6c demonstrates the effect of pH on the dye degradation varying the pH range from 3 to 9 at 60 min and 3 g/L composite weight, Degradation efficiencies of 50%, 95%, and 99% were achieved with 2.5, 5, and 10% CNF/Ag_2Se, respectively, when the pH was increased from 3 to 9. When the pH increase, the alkaline solution enhances the oxidation rate and great quantity of OH– accessible on the surface of the catalysts was achieved. Thus, MB (cationic dye) degradation was enhanced in the alkaline medium. The highest drgredation was noticed at pH 9 indicating that pH 9 is the optimum pH for that degradation reaction. However, at pH > 9, full saturation of the surface of the catalyst by MB occurred which hinders the availability for adsorption and reducing photocatalytic activity [5] as well as at pH > 9 the dye become faint and lost its chromophore. However, in the acidic pH range MB dye undergo repulsion with the catalyst surface preventing the arrival of dye to its surface. Thus, the decolorization efficiency was lower in the acidic pH range [55, 56].

UV–Visible investigation of the degradation process as a function of illumination time was performed during a photocatalytic experiment using 10% CNF/Ag_2Se (the composite with the highest photodegradation rate among all prepared composites) under the preset optimal conditions as shown in Fig. 6d which confirms the gradual degradation of MB as a function of time.

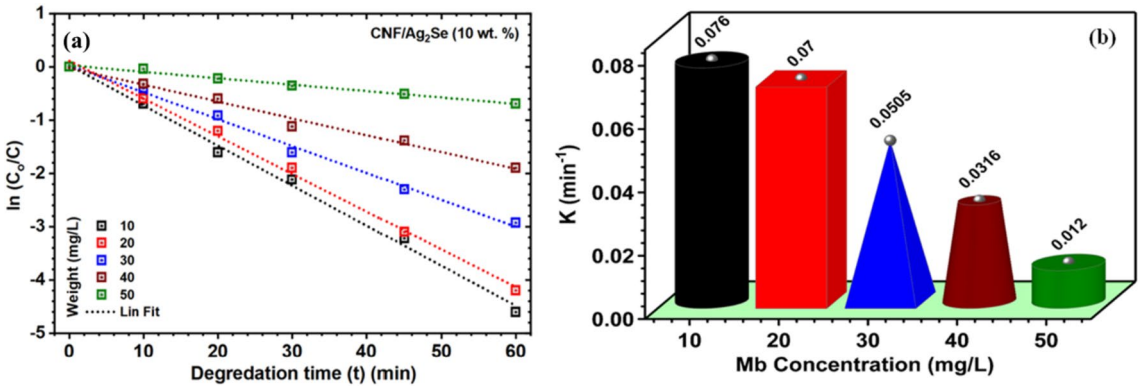

Fig. 7 **a** Pseudo-first-order kinetics for the degradation of different concentrations of MB and **b** the effects of different MB concentrations on the photodegradation reaction rate for 10% CNF/Ag_2Se composites

$$kt = \ln\left(\frac{C}{C_o}\right) \tag{9}$$

where k (min^{-1}) is the rate constant, t (min) is the irradiation period, Co is the initial concentration of MB, and C is the concentration of MB that remains after a given irradiation time [57]. Different concentrations of MB were used in the photocatalytic experiments, and the results are shown in Fig. 7a. Using linear regression, the rate constants were calculated for MB photodegradation using 10% CNF/Ag_2Se (the composite with the highest photodegradation rate among all created composites) during 60 min of simulated sunlight irradiation (3 g/L composite weight and pH 9). Since lnC/Co is directly proportional to time, we may infer that the photocatalytic degradation reaction is likewise a pseudo first-order reaction. The higher the concentration of MB, the slower the degradation rate constant becomes. The lack of light penetration and subsequent photocatalytic activity is depicted in Fig. 7b because of the high concentration of the dye solution.

To determine which species, play a significant role in the degradation of MB on the surface of 10% CNF/Ag_2Se composite, a radical trapping experiment was carried out. Photogenerated OH radicals and holes were captured using two scavengers: ethanol and EDTA. When EDTA was present, the photogenerated holes were confined, resulting in a marked decrease in the rate of MB photodegradation (Fig. 8a). The photodegradation was slightly reduced by adding ethanol because the photogenerated OH radical was inhibited. Consequently, holes may be the primary active species in the photocatalytic degradation of MB dye utilizing CNF/Ag_2Se composite (Eq. 10–15).

$$CNF/Ag_2Se + h\upsilon \rightarrow Ag_2Se/CNF\left(e_{cb-} + h_{vb}\right) \tag{10}$$

$$CNF/Ag_2Se\left(e_{cb-}\right) + O_2 \rightarrow Ag_2Se/CNF + O_2^{\cdot -} \tag{11}$$

$$h^+ + H_2O \rightarrow OH^{\cdot} + H \tag{12}$$

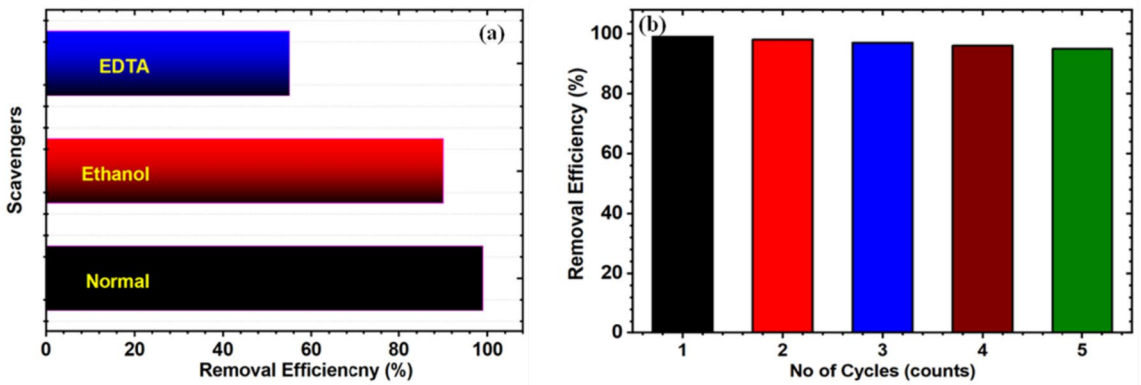

Fig. 8 **a** The effect of adding scavenger on the % removal of MB dye, **b** Reusability study of 10% CNF/Ag_2Se composite for the degradation of MB under optimal conditions

$$e^- + O_2 \rightarrow O_2^{\cdot -} \quad (13)$$

$$h_{vb+} + \text{dye} \rightarrow \text{degradation byproduct} \quad (14)$$

$$\text{dye} \rightarrow \text{degradation byproduct} \quad (15)$$

To test the recyclability of the CNF/Ag_2Se composite in the degradation of MB, the film was simply removed off the reaction mixture, cleaned, and dried for reuse. MB can be recycled successfully with an appropriate degradation process. Catalytic performance of the CNF/Ag_2Se composite was maintained even after 5 cycles of use, as illustrated in Fig. 8b.

To identify the mineralization after the degradation of methylene blue, GC–MS study carried out at the end of the photocatalytic degradation of MB using 10% CNF/Ag_2Se composite under the optimum operating conditions Fig. By comparing the byproducts of MB decolorization with data from the NIST, WILLY library of the GC/MS system, the byproducts' relative retention times and mass spectra were determined aligned to the previous studies, The core imino-group (N=C) of MB was attacked by active radicals, leading to double bond cleavage and the formation of C16H21N3SO (m/z = 303). Then, the –S = group in the para position of the central aromatic ring is cleaved, resulting in a substituted aniline as shown for products at m/z = 189, 201.2 [58, 59] (Fig. 9). Short chain acids like acetic acid, oxalic acid, and succinic acid were created when benzene rings were broken down. Inorganic compounds such carbon dioxide, water, nitrate, and sulfate were the end result of short-chain acids' mineralization [55, 56]

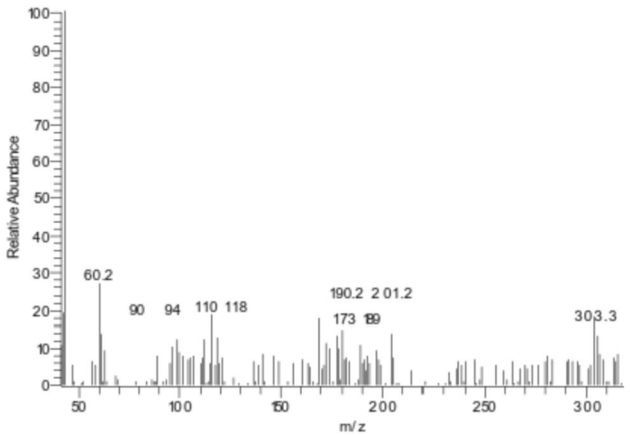

Fig. 9 Photocatalytic degradation of MB with 10% CNF/Ag_2Se at optimal conditions as detected by GC–MS mass spectrometry

The toxicity of the treated water with 10% CNF/Ag_2Se was determined by incubating a solution of 107 cell/mL Vibrio Fischeri organism at pH 7 for 10 min while subjecting it to intense light. A control sample was also routinely given treatment at the same time. There was no discernable distinction between the control and Vibrio Fischeri samples. The Microtox EC50 value of > 100 mg/L demonstrated that the 10% CNF/Ag_2Se treated water was nontoxic, verifying the safe nature of the treated water [60].

Factorial Design (Experimental Design)

Applying statistical data analysis of the factorial design results were estimated to determine the significance between and within the low and the high levels of each factor for photocatalytic activity of 10% CNF/Ag_2Se Table 2 the 24 factorial designs can be used to produce a mathematical model containing a maximum of 16 parameters, which each one of them is related to the 16 possible effects described. As well as Pareto chart, was plotted and interpreted in Fig. 9.

Pareto Chart The values of the main and the interaction effects were expressed in the Pareto chart plot (Fig. 10) and represented by the horizontal columns. The t-value revealed by the vertical line "reference line" existed on the graph indicated the minimum statistical significance at 95% confidence levels. Values that exceed the reference line were significant values while others not exceed the line were non-significant values [61]. The Pareto chart of 10% CNF/Ag_2S demonstrated t-value equal 2.2 indicated that the irradiation time and the dye concentration were the effective values which coincide with the effect of irradiation time on the percent removal of MB for 10% CNF/Ag_2S since the removal% of MB at 10 min irradiation time was 40% and this value recorded 99% at 60 min irradiation time (Fig. 6c). Moreover, the removal% of MB for 10% CNF/Ag_2Se at 10 mg/L MB dye was 99% and attained 25% at 50 mg/L dye concentration. Thus, irradiation time and dye concentration has

Table 2 Factorial design low and the high levels of each factor affecting the photocatalytic activity of 10% CNF/Ag_2Se

Name	Units	Type	Changes	SD	Low	High
Time	min	Factor	Easy	0	10	60
Film weight	glL	Factor	Easy	0	1	3
pH	–	Factor	Easy	0	3	9
Dye conc	mglL	Factor	Easy	0	10	50

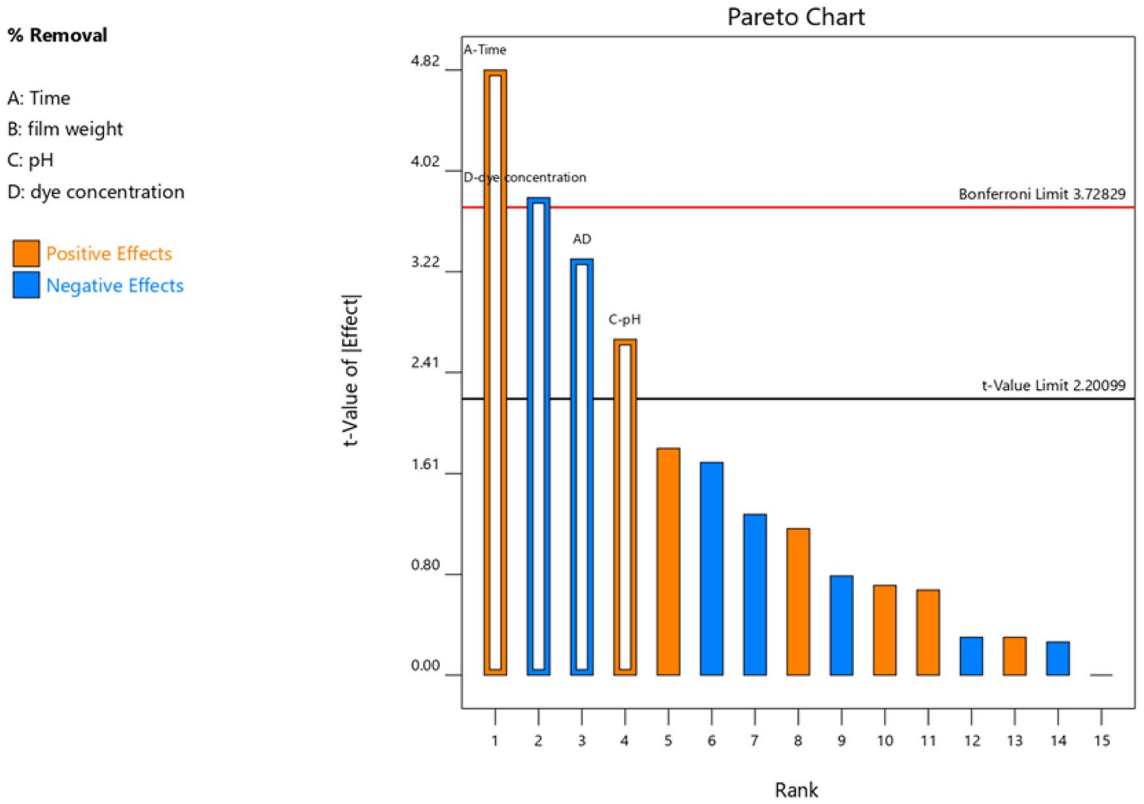

Fig. 10 Pareto chart for the degradation of MB under optimal conditions for 10%Ag_2Se/CNF composite

Table 3 Factor affecting the photocatalytic activity of 10% CNF/Ag_2Se and their variance inflation factors

Factor	Coefficient Estimate	Df	Standard Error	95% CI Low	95% CI High	VIF
Intercept	22.63	1	3.32	15.32	29.93	–
A-Time	16.00	1	3.32	8.70	23.30	1.00
C-pH	8.88	1	3.32	1.57	16.18	1.00
D-dye conc	− 12.63	1	3.32	− 19.93	− 5.32	1.00
AD	− 11.00	1	3.32	− 18.30	− 3.70	1.00

Table 4 Factors influencing the photocatalytic activity of 10% CNF/Ag_2Se and their corresponding significance

Source	Sum of squares × 10^3	df	Mean square	F-value	P-value	Significance
Model	9.84	4.00	2460.63	13.97	0.0003	Significant
A-Time	4.09	1.00	4096.00	23.26	0.0005	–
C-pH	1.26	1.00	1260.25	7.16	0.0216	–
D-dye Conc	2.55	1.00	2550.25	14.48	0.0029	–
AD	1.94	1.00	1936.00	10.99	0.0069	–
Residual	1.93	11.00	176.11	–	–	–
Cor Total	11.77	15.00	–	–	–	–

been approved as the significant factors that influenced the removal of MB using 10% CNF/Ag_2S.

ANOVA Analysis for Selected Factorial Model Analysis of variance (ANOVA) was estimated to determine the significance between factors and within the low and the high

levels of each factor (Table 3). Two levels that allowed us to have enough powder from each sample to perform all the 16 required experiments were chosen and Coefficients in Terms of Coded Factors were displayed in Table 4. The coefficient represents the expected change in response per unit change in factor value when all remaining factors are held constant. The intercept in an orthogonal design is the overall average response of all the runs. The coefficients are adjustments around that average based on the factor settings. When the factors are orthogonal the VIFs (variance inflation factors) are 1; VIFs greater than 1 indicate multi-collinearity, the higher the VIF the more severe the correlation of factors (Table 3). As a rough rule, VIFs less than 10 are tolerable. The model is suggested to be significant by the model's F-value of 13.97. An F-value this large might happen because of noise only 0.03% of the time. Model terms are considered significant when the P-value is less than 0.0500. In this instance, key model terms include A, C, D, and AD. Model terms are not significant if the value is higher than 0.1000. Model reduction may enhance your model if it has a lot of unnecessary terms (except those needed to maintain hierarchy). The Predicted R^2 of 0.6521 is in reasonable agreement with the Adjusted R^2 of 0.7757; i.e., the difference is less than 0.2. Adeq Precision measures the signal to noise ratio. A ratio greater than 4 is desirable. Your ratio of 10.110 indicates an adequate signal. This model can be used to navigate the design space.

Final Equation in Terms of Coded Factors It is possible to anticipate the response for specific levels of each factor using the equation expressed in terms of coded factors. By default, the factors' high levels are coded as + 1 and their low levels as − 1. By comparing the factor coefficients, the coded equation can be used to determine the relative importance of the elements. Figure 11a represents the interaction between factors and their effect on the removal%, where A: Time and D: Dye concentration as well as Fig. 11b which represents the interaction between factors and their effect on the removal% A: Time and B: film weight.

$$\%\ \text{Removal} = 22.63 + 16A + 8.88C - 12.63Dx11AD \quad (16)$$

Sustainability Aspects of the Prepared Catalyst and Procedure

Sustainable materials and processes should consider material, economy, design, market, equity, technology, and ecology. Environmental, social, and economic sustainability are based on these principles. This approach meets most of these criteria:

1. Material: Ag_2Se and CNF are abundant, eco-friendly basic materials. Ag_2Se, a silver selenide with low toxicity, is ideal for green processes. Cellulose, a sustainable biopolymer, is the most common specially, cellulose nanofibers were synthesized from bleached bagasse pulp by TEMPO-oxidation. Thus, CNF/Ag_2Se composite exhibits long-term performance.
2. Cost-effectiveness: Both raw materials are regularly available and affordable, which makes them excellent candidates for use. In addition, since sunlight is a free

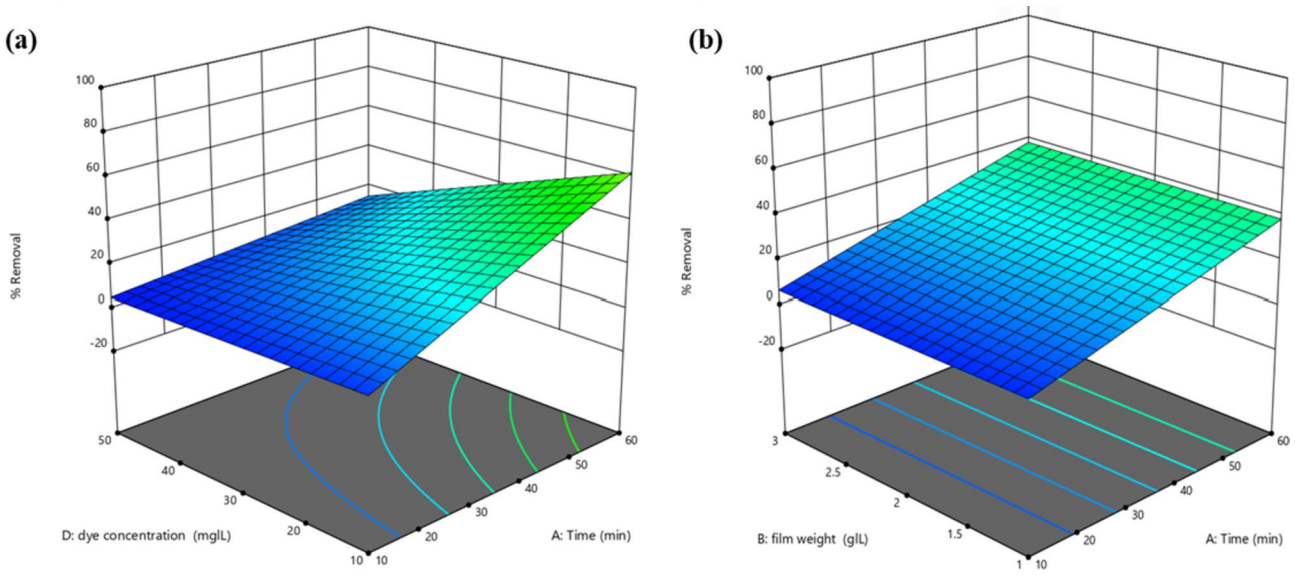

Fig. 11 **a** The interaction between factors and their effect on the % removal A: Time and D: Dye concentration, **b** represents the interaction between factors and their effect on the % removal A: Time and B: film weight

source of energy, the process's start-up and operating expenses will be lower.
3. Design: Because the catalyst is produced on cellulose-based material, CNF is recyclable and has a low environmental impact.
4. Market: This study will be a method that can be locally deployed everywhere with minimum equipment thanks to the use of sunlight as the source of energy.
5. Equity: Locally applicable, low impact technology that reduces local issues
6. Technology: Catalyst production is a novel process that features new technology.
7. Ecology: The manufacturing process was a low toxicity process that used almost no harmful materials to eliminate harmful pollutants in the water. The technology was also evaluated by conducting photodegradation tests under sunlight and developed by improving the efficiency using optimized catalysts. Step for implementation of photocatalysis process in large-scale water treatment is immobilization of photo catalyst in suitable matrix to combat nanoparticle release into the environment that creates secondary contaminants and to overcome the challenge for reusability of the photo catalyst. As a result, these aspects suggest that this study is geared toward sustainability.

Conclusion

In this study, CNF/Ag_2Se composites were successfully fabricated by in situ synthesis of Ag_2Se nanoparticles in the structure of CNF which were synthesized from bleached bagasse pulp by TEMPO-oxidation. The results showed that the prepared submicrosize Ag_2Se particles with a narrow size distribution were homogeneously dispersed in the CNF. The prepared composites were characterized by XRD that demonstrated that the prepared Ag_2Se has been formed in single-phase orthorhombic β-Ag_2Se. Band gap measurements have been calculated and found to be reduced from 4.61 to 2.71 eV, demonstrating the efficiency of polymeric films under visible-driven-light photocatalytic activity. Methylene blue (MB) degradation was used to test the composite's photocatalytic efficacy, as it is a model compound of an organic contaminant found in wastewater. Results show that 10% CNF/Ag_2Se exhibited the maximum photocatalytic activity under simulated sunlight for 60 min, pH 9, and 3 g/L of composite weight, and maintained a good photocatalytic stability after recycling numerous times. Based on the statistical analysis of the factorial design data, the irradiation time and the dye concentration have the greatest impact on the photodegradation of MB dye. Most sustainability criteria are met by this study: environmental, social, and economic, as well as, considered step for implementation of photocatalysis process in large-scale water treatment process.

Acknowledgements The authors acknowledge the National Research Center for financial support.

Author Contributions Talaat A. Hameed and Ahmed Salama conceptualized the work and prepared the materials. Rabab A. Nasr performed the Photocatalytic degradation section. All authors carried out the analyses, discussion, and revisions equally.

Funding Open access funding provided by The Science, Technology & Innovation Funding Authority (STDF) in cooperation with The Egyptian Knowledge Bank (EKB). The authors have not disclosed any funding.

Declarations

Conflict of interest The authors declare that they have no conflict of interest.

References

1. Guo J, Khan S, Cho S-H, Kim J (2019) Preparation and immobilization of zinc sulfide (ZnS) nanoparticles on polyvinylidene fluoride pellets for photocatalytic degradation of methylene blue in wastewater. Appl Surf Sci 473:425–432. https://doi.org/10.1016/j.apsusc.2018.12.103
2. Mills A, Le Hunte S (1997) An overview of semiconductor photocatalysis. J Photochem Photobiol A Chem 108:1–35. https://doi.org/10.1016/S1010-6030(97)00118-4
3. Zhong W, Xu J, Wang P et al (2022) Novel core-shell Ag@AgSe nanoparticle co-catalyst: in situ surface selenization for efficient photocatalytic H_2 production of TiO_2. Chin J Catal 43:1074–1083. https://doi.org/10.1016/S1872-2067(21)63969-4
4. Dursun S, Akyildiz H, Kalem V (2021) PMN-PT nanoparticle/SnO_2 nanofiber heterostructures: enhanced photocatalytic degradation performance by ultrasonic wave induced piezoelectric field. J Alloys Compd 889:161769. https://doi.org/10.1016/j.jallcom.2021.161769
5. Rahman A, Khan MM (2021) Chalcogenides as photocatalysts. New J Chem 45:19622–19635. https://doi.org/10.1039/D1NJ04346C
6. Li J, Jiménez-Calvo P, Paineau E, Ghazzal MN (2020) Metal chalcogenides based heterojunctions and novel nanostructures for photocatalytic hydrogen evolution. Catalysts 10:89. https://doi.org/10.3390/catal10010089
7. Dursun S, Akyıldız H, Kalem V (2023) Production of $CuCoO_2$ nanoparticle/SnO_2 nanofiber heterostructures for visible light

photocatalytic applications. J Photochem Photobiol A Chem 434:114233. https://doi.org/10.1016/j.jphotochem.2022.114233
8. Dursun S, Kaya İC, Kocabaş M et al (2020) Visible light active heterostructured photocatalyst system based on CuO platelike particles and SnO_2 nanofibers. Int J Appl Ceram Technol 17:1479–1489. https://doi.org/10.1111/ijac.13467
9. Dursun S, Sarıipek FB, Kılıç S et al (2023) Investigation of photocatalytic activity (under visible light) of ultrathin CZTS films produced in different thicknesses by PLD method. Opt Quantum Electron 55:166. https://doi.org/10.1007/s11082-022-04417-w
10. Wang Y, Ren B, Zhen OuJ et al (2021) Engineering two-dimensional metal oxides and chalcogenides for enhanced electro- and photocatalysis. Sci Bull 66:1228–1252. https://doi.org/10.1016/j.scib.2021.02.007
11. Hameed TA, Sharmoukh W, Anis B, Youssef AM (2022) Enhanced photocatalytic activity and diode performance of ZnO-GO nanocomposites via doping with aluminum. Int J Energy Res 46:22601–22624. https://doi.org/10.1002/er.8563
12. Shaban H, Gad SA, Mansour BA et al (2020) The influence of substrate temperatures and thickness on optical and electrical conductivity of $CuIn(Se_{0.25}S_{0.75})_2$. J Inorg Organomet Polym Mater 30:1360–1368. https://doi.org/10.1007/s10904-019-01267-0
13. Nie L, Zhang Q (2017) Recent progress in crystalline metal chalcogenides as efficient photocatalysts for organic pollutant degradation. Inorg Chem Front 4:1953–1962. https://doi.org/10.1039/C7QI00651A
14. Pei Y-L, Liu Y (2012) Electrical and thermal transport properties of Pb-based chalcogenides: PbTe, PbSe, and PbS. J Alloys Compd 514:40–44. https://doi.org/10.1016/j.jallcom.2011.10.036
15. Dong H, Chen Y-C, Feldmann C (2015) Polyol synthesis of nanoparticles: status and options regarding metals, oxides, chalcogenides, and non-metal elements. Green Chem 17:4107–4132. https://doi.org/10.1039/C5GC00943J
16. Hasan S, Baral K, Li N, Ching W-Y (2021) Structural and physical properties of 99 complex bulk chalcogenides crystals using first-principles calculations. Sci Rep 11:9921. https://doi.org/10.1038/s41598-021-89281-6
17. Salman Khan M, Gul B, Khan G et al (2023) The physical properties of RbAuX (X = S, Se, Te) novel chalcogenides for advanced optoelectronic applications: an ab-initio study. Comput Mater Sci 221:112098. https://doi.org/10.1016/j.commatsci.2023.112098
18. Ashery A, Elnasharty MMM, Hameed TA (2020) Investigation of electrical and dielectric properties of epitaxially grown Au/n-GaAs/p-Si/Al heterojunction. Opt Quantum Electron 52:490. https://doi.org/10.1007/s11082-020-02601-4
19. Shi Y, Sturm C, Kleinke H (2019) Chalcogenides as thermoelectric materials. J Solid State Chem 270:273–279. https://doi.org/10.1016/j.jssc.2018.10.049
20. Mallah A, Debbichi M, Dhaou MH, Bellakhdhar B (2023) Structural, mechanical, and piezoelectric properties of Janus bidimensional monolayers. Crystals 13:126. https://doi.org/10.3390/cryst13010126
21. Nair N, Sankapal BR (2023) 0D, 1D, 2D, and 3D structured chalcogenides for supercapacitor applications. Chemically deposited metal chalcogenide-based carbon composites for versatile applications. Springer, Cham, pp 1–52
22. Wu Z, Ou Y, Cai M et al (2023) Short-wave infrared photodetectors and imaging sensors based on lead chalcogenide colloidal quantum dots. Adv Opt Mater 11:2201577. https://doi.org/10.1002/adom.202201577
23. Munonde TS, Nomngongo PN (2023) Review on metal chalcogenides and metal chalcogenide-based nanocomposites in photocatalytic applications. Chem Africa 6:1127–1143. https://doi.org/10.1007/s42250-022-00577-0
24. Tayyab M, Liu Y, Liu Z et al (2023) A new breakthrough in photocatalytic hydrogen evolution by amorphous and chalcogenide enriched cocatalysts. Chem Eng J 455:140601. https://doi.org/10.1016/j.cej.2022.140601
25. Wang H, Yuan X, Wang H et al (2016) Facile synthesis of Sb2S3/ultrathin g-C_3N_4 sheets heterostructures embedded with g-C_3N_4 quantum dots with enhanced NIR-light photocatalytic performance. Appl Catal B Environ 193:36–46. https://doi.org/10.1016/j.apcatb.2016.03.075
26. Ma X, Li W, Ren C et al (2021) A novel noble-metal-free binary and ternary In_2S_3 photocatalyst with WC and "W-Mo auxiliary pairs" for highly-efficient visible-light hydrogen evolution. J Alloys Compd 875:160058. https://doi.org/10.1016/j.jallcom.2021.160058
27. Kudo A, Sekizawa M (2000) Photocatalytic H_2 evolution under visible light irradiation on Ni-doped ZnS photocatalyst. Chem Commun. https://doi.org/10.1039/b003297m
28. Wang L, Cheng B, Zhang L, Yu J (2021) In situ irradiated XPS investigation on S-scheme TiO_2 @$ZnIn_2S_4$ photocatalyst for efficient photocatalytic CO_2 reduction. Small 17:2103447. https://doi.org/10.1002/smll.202103447
29. Hao X, Shao Y, Xiang D, Jin Z (2022) Photocatalytic overall water splitting hydrogen production over ZnCdS by spatially-separated WP and Co_3O_4 cocatalysts. Sol Energy Mater Sol Cells 248:111970. https://doi.org/10.1016/j.solmat.2022.111970
30. Chen D, Ye J (2007) Photocatalytic H_2 evolution under visible light irradiation on $AgIn_5S_8$ photocatalyst. J Phys Chem Solids 68:2317–2320. https://doi.org/10.1016/j.jpcs.2007.07.059
31. Peng Y, Zhu Q, Xu W, Cao J (2022) High anisotropic optoelectronics in monolayer binary M8X12 (M = Mo, W; X = S, Se, Te). ACS Appl Mater Interfaces 14:27056–27062. https://doi.org/10.1021/acsami.2c05169
32. Murugesan P, Moses JA, Anandharamakrishnan C (2019) Photocatalytic disinfection efficiency of 2D structure graphitic carbon nitride-based nanocomposites: a review. J Mater Sci 54:12206–12235. https://doi.org/10.1007/s10853-019-03695-2
33. Xu J, Zhang C, Liu H et al (2020) Amorphous MoOX-Stabilized single platinum atoms with ultrahigh mass activity for acidic hydrogen evolution. Nano Energy 70:104529. https://doi.org/10.1016/j.nanoen.2020.104529
34. Yang S, Zhang H, Zhang J, Zhou X (2022) A novel route for preparing Ag_2Se-based micro-nanocomposites and their photocatalytic activity. J Nanopart Res 24:170. https://doi.org/10.1007/s11051-022-05546-9
35. Lei P, Wang F, Gao X et al (2012) Immobilization of TiO_2 nanoparticles in polymeric substrates by chemical bonding for multicycle photodegradation of organic pollutants. J Hazard Mater 227–228:185–194. https://doi.org/10.1016/j.jhazmat.2012.05.029
36. Wang C, Shi Z, Peng L et al (2017) Preparation of carbon foam-loaded nano-TiO_2 photocatalyst and its degradation on methyl orange. Surf Interfaces 7:116–124. https://doi.org/10.1016/j.surfin.2017.03.007
37. Salama A (2017) Dicarboxylic cellulose decorated with silver nanoparticles as sustainable antibacterial nanocomposite material. Environ Nanotechnol Monit Manag 8:228–232. https://doi.org/10.1016/j.enmm.2017.08.003
38. Salama A, Hesemann P (2020) Recent trends in elaboration, processing, and derivatization of cellulosic materials using ionic liquids. ACS Sustain Chem Eng 8:17893–17907. https://doi.org/10.1021/acssuschemeng.0c06913
39. Abdelrazek EM, Abdelghany AM, Badr SI, Morsi MA (2018) Structural, optical, morphological and thermal properties of PEO/PVP blend containing different concentrations of biosynthesized Au nanoparticles. J Mater Res Technol 7:419–431. https://doi.org/10.1016/j.jmrt.2017.06.009

40. Salama A, Abou-Zeid RE, Cruz-Maya I, Guarino V (2020) Soy protein hydrolysate grafted cellulose nanofibrils with bioactive signals for bone repair and regeneration. Carbohydr Polym 229:115472. https://doi.org/10.1016/j.carbpol.2019.115472
41. El-Sayed NS, Salama A, Guarino V (2022) Coupling of 3-aminopropyl sulfonic acid to cellulose nanofibers for efficient removal of cationic dyes. Materials (Basel) 15:6964. https://doi.org/10.3390/ma15196964
42. Palaporn D, Mongkolthanaruk W, Faungnawakij K et al (2022) Flexible thermoelectric paper and its thermoelectric generator from bacterial cellulose/Ag_2Se nanocomposites. ACS Appl Energy Mater 5:3489–3501. https://doi.org/10.1021/acsaem.1c04042
43. Cullity BD (1956) Elements of X ray diffraction. Addison-Wesley Publishing Company, Inc.
44. Carvalho MH, Pereira EC, de Oliveira AJA (2018) Orthorhombic SnO_2 phase observed composite $(Sn_{1-x}Ce_x)O_2$ synthesized by sol–gel route. RSC Adv 8:3958–3963. https://doi.org/10.1039/C7RA12727H
45. Chen W, Cao W, Hameed TA et al (2015) Properties of Cu(In, Ga, Al)Se_2 thin films fabricated by pulsed laser deposition. J Mater Sci Mater Electron 26:1743–1747. https://doi.org/10.1007/s10854-014-2602-y
46. Hameed TA, Mohamed F, Turky G, Salama A (2022) Carboxymethylcellulose/polyvinylpyrrolidone filled with Al-doped ZnO nanoparticles as a promising film for optoelectronic applications. Opt Mater (Amst) 134:113097. https://doi.org/10.1016/j.optmat.2022.113097
47. Mohamed F, Ahmad MM, Hameed TA (2023) Greener synthesis of lightweight, self-standing PMMA/$CoFe_2O_4$ polymeric film for magnetic, electronic, and terahertz shielding applications. Polym Adv Technol 34:1497–1514. https://doi.org/10.1002/pat.5984
48. Hameed TA, Cao W, Mansour BA et al (2015) Properties of Cu(In, Ga, Al)Se_2 thin films fabricated by magnetron sputtering. J Vac Sci Technol A Vacuum Surf Film 10(1116/1):4913863
49. Pervaiz M, Ur Rehman M, Ali F et al (2023) Biomolecule protective and photocatalytic potential of cellulose supported MoS_2/GO nanocomposite. Bioinorg Chem Appl 2023:1–11. https://doi.org/10.1155/2023/3634726
50. Sun Z, Luo Y, Chen C et al (2024) Mechanical enhancement of carbon fiber-reinforced polymers: from interfacial regulating strategies to advanced processing technologies. Prog Mater Sci 142:101221. https://doi.org/10.1016/j.pmatsci.2023.101221
51. Abbasi M, Rafique U, Murtaza G, Ashraf MA (2018) Synthesis, characterisation and photocatalytic performance of ZnS coupled Ag_2S nanoparticles: a remediation model for environmental pollutants. Arab J Chem 11:827–837. https://doi.org/10.1016/j.arabjc.2017.12.017
52. Goswami M, Baruah D, Das AM (2018) Green synthesis of silver nanoparticles supported on cellulose and their catalytic application in the scavenging of organic dyes. New J Chem 42:10868–10878. https://doi.org/10.1039/C8NJ00526E
53. Mishra S, Du D, Jeanneau E et al (2016) A facile molecular precursor-based synthesis of Ag_2Se nanoparticles and its composites with TiO_2 for enhanced photocatalytic activity. Chem Asian J 11:1658–1663. https://doi.org/10.1002/asia.201600157
54. Abbas HA, Nasr RA, Vannier R-N, Jamil TS (2022) Improving of photocatalytic activity of barium ferrate via bismuth and copper co-doping for degradation of paracetamol under visible light irradiation. J Environ Sci 112:331–342. https://doi.org/10.1016/j.jes.2021.05.008
55. Abbas HA, Nasr RA, Khalaf A et al (2020) Photocatalytic degradation of methylene blue dye by fluorite type $Fe_2Zr_{2-x}W_xO_7$ system under visible light irradiation. Ecotoxicol Environ Saf 196:110518. https://doi.org/10.1016/j.ecoenv.2020.110518
56. Jing H-P, Wang C-C, Zhang Y-W et al (2014) Photocatalytic degradation of methylene blue in ZIF-8. RSC Adv 4:54454–54462. https://doi.org/10.1039/C4RA08820D
57. Meng Z-D, Zhu L, Ghosh T et al (2012) Ag_2Se-graphene/TiO_2 nanocomposites, sonochemical synthesis and enhanced photocatalytic properties under visible light. Bull Korean Chem Soc 33:3761–3766. https://doi.org/10.5012/bkcs.2012.33.11.3761
58. Rong P, Jiang Y-F, Wang Q et al (2022) Photocatalytic degradation of methylene blue (MB) with Cu_1–ZnO single atom catalysts on graphene-coated flexible substrates. J Mater Chem A 10:6231–6241. https://doi.org/10.1039/D1TA09954J
59. Wang X, Han S, Zhang Q et al (2018) Photocatalytic oxidation degradation mechanism study of methylene blue dye waste water with GR/iTO_2. MATEC Web Conf 238:03006. https://doi.org/10.1051/matecconf/201823803006
60. Augusta Ajuzieogu C, Obukowho Odokuma L, Chioma Blaise C (2018) Toxicity assessment of produced water using microtox rapid bioassay. South Asian J Res Microbiol. https://doi.org/10.9734/sajrm/2018/v1i4826
61. Nasr RA, Abbas HA, Vannier R-N, Jamil TS (2022) Preparation, characterization and photocatalytic decolorization process for the removal of orange–green dye using perovskites $Ba_{1-x}Bi_xFeO_{3-\delta}$ (x = 0, 0.05, 0.1). Inorg Nano-Metal Chem 52:1123–1133. https://doi.org/10.1080/24701556.2021.1958844